PLEASE CITE THIS ARTICLE AS DOI: 10.1063/5.0281503

## Statistical Inference of Higher-Order Moments of Electron Velocity Distribution Functions from Incoherent Thomson Scattering Spectra

Julian Lopez-Uricoechea, Mitchell L. R. Walker

Georgia Institute of Technology, Atlanta, GA, 30332, U.S.A

## Abstract

Noninvasive direct measurements of higher-order moments of the electron velocity distribution function (EVDF) are needed to improve the understanding of non-Maxwellian electron behavior in various plasmas. This work presents a Bayesian inference method with Monte Carlo sampling to infer the electron heat flux and excess kurtosis from ILTS spectra, which also improves the inferences of the lowerorder moments. The method assumes that the EVDFs are described by the sum of at most four super-Gaussians and is tested against synthetic spectra that are representative of ITLS measurements in lowtemperature plasmas. 15 synthetic spectra are considered that include Maxwellian, Druyvesteyn, and Kappa distributions and their skewed counterparts. For all synthetic spectra considered, the true value of the heat flux is within the uncertainty bounds of the inference. Regarding the excess kurtosis, the true value of the excess kurtosis is within the uncertainty bounds of the inference for all cases except for the Kappa distributions with no or low skewness. At the signal-to-noise ratio of the synthetic spectra, the minimum detectable skewness and excess kurtosis are around  $\pm$  0.006 and  $\pm$  0.07, respectively. When the heat flux and excess kurtosis are significantly above their minimum detectable values, relative uncertainties range between 40% and 5%. Lastly, in terms of symmetric or low-skewness EVDFs, we find that ILTS is best suited for EVDFs with negative excess kurtosis, suggesting that ILTS can accurately and precisely measure nonequilibrium electron properties in many low-temperature plasmas.

## 1. Introduction

In low-temperature plasmas, electrons can often be in non-equilibrium [1]. Such nonequilibrium can produce significant deviations from Maxwellian electron velocity distribution functions (EVDFs). Non-Maxwellian EVDFs can result in reaction rates [1-3] and fluxes through sheaths [4, 5] that differ significantly from those calculated assuming Maxwellian EVDFs and in non-conductive electron heat fluxes [6-8]. These non-Maxwellian effects can significantly influence plasma composition and spatial distributions of electron temperature [9]. While various simulation methods can capture non-Maxwellian electron effects [2-4, 7, 8, 10, 11], experimental methods are needed to validate simulations and to improve

understanding of non-Maxwellian electron behavior in different plasmas.

Langmuir probes are the most common technique used to measure non-Maxwellian electron energy distribution functions (EEDFs) [12-14], and optical emission spectroscopy (OES) has also been used to measure EEDFs [15-18]. Langmuir probes are able to measure the EEDF from low to high electron energies (0-50 eV) [1] and strategies exist to mitigate probe perturbation in certain discharges [12]. However, perturbation from Langmuir probes can be significant [19] and adds ambiguity to the results, even if the perturbation is reduced. On the other hand, while OES is non-invasive, it suffers from reduced spatial resolution as it provides spatiallyaveraged measurements across the line of sight of the diagnostic, and OES cannot measure the low-

PLEASE CITE THIS ARTICLE AS DOI: 10.1063/5.0281503

energy part of the EEDF [1]. Additionally, measurements of the EEDF cannot be used to calculate odd moments of the EVDF, such as components of the electron drift velocity and electron heat flux vectors.

Incoherent laser Thomson scattering (ILTS) can non-invasively measure the one-dimensional EVDF with high spatial resolution, but ILTS has poor signal-to-noise ratio (SNR) in the tails of the EVDF. As a result, ILTS has not been used extensively for non-Maxwellian studies in lowtemperature plasmas. Refs. 20-23 used ILTS to measure non-Maxwellian EVDFs in lowtemperature plasmas. In addition, Refs. 22 and 24 showed that incorrectly assuming a Maxwellian can produce inaccurate measurements of electron density, drift velocity, and temperature. However, there are two important gaps in the approach to analyzing ILTS measurements of non-Maxwellian EVDFs. First, the authors are not aware of attempts to quantify uncertainty in ILTS measurements of electron density, drift velocity, and temperature that incorporate the uncertainty of the type of EVDF that best describes the data. Second, the authors are not aware of any use of ILTS to quantify the deviation from Maxwellian EVDFs. Given the low SNR in the tails of the EVDF in ILTS measurements, robust uncertainty quantification is necessary to account for the possibility of non-Maxwellian EVDFs in ILTS measurements of electron density, drift velocity, and temperature. Robust uncertainty quantification can also enable quantitative ILTS measurements of the deviation from Maxwellian EVDFs through the electron heat flux and excess kurtosis.

The methods for analyzing non-Maxwellian velocity distribution functions (VDFs) are direct integration, modeling of VDFs with a single alternative distribution, and modeling of VDFs with multiple components. When the VDF can be directly extracted from the raw measurement, as in ILTS when the width of the instrument function

negligible compared to the electron temperature, the moments of the VDF can be calculated directly through integration of the measured signal; Ref. 22 did this with an ILTS measurement of a skewed EVDF, but the main downside of this method is that it does not provide an uncertainty for the calculated moments of the VDF. Analyzing non-Maxwellian VDFs with a single alternative distribution has been done with a Druyvesteyn [23], Kappa [25], super-Gaussian [25,26,27], and skew-Gaussian [28], among others [3,29,30,31]. Analyzing non-Maxwellian VDFs with multiple components has been done with two Maxwellians [21,24,33], sum of a Maxwellian and a super-Gaussian [32], and the sum of a Maxwellian, super-Gaussian, and Kappa [34]. While alternative-distribution methods can be enhanced by Bayesian model selection [23,25], these model selection methods are inherently limited in their capability to accurately model VDFs that are not included within the models being selected. As a result, multi-component methods recreate measured VDFs more accurately than alternativedistribution methods [6]. Regarding uncertainty quantification, multi-component methods can be enhanced with Bayesian inference of the moments of the VDF following the Bayesian inference of the parameters that model the VDF [32,35]. However, the highest-order moment that these multi-component Bayesian inference methods have inferred from the VDF is the effective temperature. It is also worth noting that the electron heat flux has been directly calculated from EVDF measurements in the solar wind [36].

This work presents a Bayesian inference method to analyze non-Maxwellian EVDFs with ILTS that assumes that the EVDF is the sum of at most four super-Gaussians. The method was tested against synthetic ILTS representative of Maxwellian, Druyvesteyn, and Kappa distributions as well as skewed versions of these distributions. This study

PLEASE CITE THIS ARTICLE AS DOI: 10.1063/5.0281503

Druyvesteyn distributions as they are commonly found in low-temperature plasmas, and it includes Kappa distributions as an example of a leptokurtic distribution, since simulations of Hall thrusters have found EVDFs with positive excess kurtosis [4,8]. The main objective of the study is to demonstrate that ILTS can accurately measure the first five moments of the one-dimensional EVDF for a wide variety of EVDFs, specifically the electron density, drift velocity, electron temperature, heat flux, and excess kurtosis. Section 2 describes the Bayesian inference method and the generation of the synthetic ILTS spectra. Section 3 evaluates the accuracy of the proposed method, compares the method's accuracy to simpler methods, and explores the limits of the proposed method regarding spectral resolution and spectral range.

## 2. Methodology

## 2.1. ILTS Model Equations

Thomson scattering is the elastic scattering of light off charged particles, and in the incoherent regime, the scattered spectrum is dominated by scattering off electrons. Thomson scattering is incoherent when  $\frac{2\pi}{k} \gg \lambda_{De}$ , where k is the observation wavevector and  $\lambda_{De}$  is the Debye length. The observation wavenumber is given by

$$k = \frac{4\pi}{\lambda_i} \sin\left(\frac{\theta}{2}\right),\tag{1}$$

where  $\lambda_i$  is the laser's incident wavelength and  $\theta$  is the scattering angle.

The spectral density of the signal measured by ILTS as function of wavelength is

$$P_s(\lambda) = \frac{c\sigma_T \Delta \lambda n_e}{k} \left[ I_s(\lambda) * \hat{f}_k(\nu) \right], \tag{2}$$

where C is the calibration constant provided by laser Raman scattering (LRS) [37],  $\sigma_T$  is the Thomson scattering cross section [38],  $\Delta\lambda$  is the spectral resolution of the ILTS spectrum,  $n_e$  is the electron density, k is the observation wavenumber,  $I_S(\lambda)$  is the normalized ( $\Delta\lambda \sum I_S =$ 

1) instrument function of the detection system and needs to be measured separately,  $\hat{f}_k$  is the one-dimensional normalized EVDF along the observation wavevector, and \* denotes a discrete convolution. v, the electron velocity corresponding to a given wavelength, is given by

$$v(\lambda) = \frac{2\pi c}{k} \left( \frac{1}{\lambda_i} - \frac{1}{\lambda} \right),\tag{3}$$

when using the observation wavevector convention of  $\vec{k} = \vec{k}_i - \vec{k}_s$ , where  $\vec{k}_i$  is the incident wavevector and  $\vec{k}_s$  is the scattering wavevector.  $f_k = n_e \hat{f}_k$  is defined as the sum of four super-Gaussians,

$$f_k(v) = \sum_{i=1}^4 f_i^{SG}(v)$$
 (4)

where a super-Gaussian is defined as

$$f_i^{SG}(v) = A_i \exp\left(-\left|\frac{v - v_{D,i}}{\Delta v_i}\right|^{b_i}\right), \tag{5}$$

To simplify the numerical implementation of the model equations, the problem is regularized in two ways. First,  $v_{D,i}$  and  $\Delta v_i$  are expressed in Mm/s, such that  $[f_k] \sim \frac{s}{Mm^2}$ . Second,  $\log_{10} A_i$  were used as model parameters instead of  $A_i$ . Third, from the recorded ILTS spectrum,  $P_S^R(\lambda)$ , the regularized recorded ILTS spectrum is defined as

$$d(\lambda) = \frac{P_s^R(\lambda)}{\max\left[\frac{P_s^R k}{\sigma_T}\right]},\tag{6}$$

and  $B = \max \left[ \frac{P_S^R k}{\sigma_T} \right]$ . The modeled regularized ILTS spectrum is then similarly defined as

$$\begin{split} M\!\left(\lambda,\vec{\theta},C,I_s\right) &= \frac{c\sigma_T\Delta\lambda n_e}{kB} \big[I_s(\lambda) * \hat{f}_k(v,\vec{\theta})\big], \ (7) \\ \text{where} \qquad &\vec{\theta} = \big[\log_{10}(A_1),\Delta v_1,v_{D,1},b_1,\dots, \\ \log_{10}(A_4),\Delta v_4,v_{D,4},b_4\big]. \end{split}$$

## 2.2. Implementation of Bayesian inference

The authors chose to implement Bayesian inference to effectively propagate the uncertainty of inferred values of  $\vec{\theta}$  to the uncertainty of the

PLEASE CITE THIS ARTICLE AS DOI: 10.1063/5.0281503

moments of  $f_k$ . Given  $d(\lambda)$  and  $I_s(\lambda)$ , the joint probability distribution of  $\vec{\theta}$  and  $\vec{\varphi}$  is given by the posterior probability distribution,  $p(\vec{\theta}, \vec{\varphi}|d, I_s)$ , where  $\vec{\varphi}$  contains the nuisance parameters. In general, nuisance parameters are parameters that need to be inferred but that are not of primary interest. The posterior probability distribution is given by Bayes rule as

$$p(\vec{\theta}, \vec{\varphi}|d, I_s) = \frac{p(d, I_s|\vec{\theta}, \vec{\varphi})p(\vec{\theta}, \vec{\varphi})}{p(d, I_s)}, \tag{8}$$

where  $p(d, I_s | \vec{\theta}, \vec{\varphi})$  is the likelihood of observing the data given a set of the model parameters,  $p(\vec{\theta}, \vec{\varphi})$  is the prior probability distribution of the model parameters, and  $p(d, I_s)$  is the evidence. The evidence does not need to be modeled because it is a normalizing constant of the posterior distribution. The likelihood constructed by assuming that the errors at each wavelength,  $e = d(\lambda) - M(\lambda, \vec{\theta}, C, I_s)$ , independent and identically distributed as  $e \sim N(0, s^2)$ .

This work uses uninformative priors for  $\theta$ , namely  $\log_{10}(A_i) \sim N(0, 10),$  $\Delta v_i \sim U \left( 420 \frac{km}{s}, 5939.7 \frac{km}{s} \right),$  $v_{D,i} \sim U\left(-2000 \frac{km}{s}, 2000 \frac{km}{s}\right),$  $b_i \sim U(1.5, 6)$ . In general, uninformative priors, such as uniform distributions and normal distributions with a large standard deviation, are used when no prior information is available on the inferred parameters. The range of values for  $\Delta v_i$  corresponds to an electron temperature range of 0.5 eV to 100 eV for Maxwellian EVDFs and can be changed depending on the expected range of electron temperature. The lower limit for  $b_i$ was set below 2 such that a single super-Gaussian could produce positive and negative excess kurtosis and at 1.5 such that that  $f_k$  for a single super-Gaussian cannot be unphysically sharp at  $v = v_D$ . The nuisance parameters are C and s. The prior distribution of C is the posterior distribution of C from Bayesian inference of preliminary LRS measurements, which can be done following the method in Ref 23. For s, the prior is  $s \sim Exp(1)$ . The total prior distribution,  $p(\vec{\theta}, \vec{\varphi})$ , is simply the product of all the individual priors.

Monte Carlo sampling was used to calculate  $p(\vec{\theta}, \vec{\varphi}|d, I_s)$  numerically. Specifically, the NumPyro Python package was used to preliminarily transform the posterior distribution to a Gaussian-like one with a trained autoguide and then implement a No-U-Turn sampler (NUTS) to sample from the transformed posterior distribution, as described in Ref. 39 and implemented in the "Neural Transport" NumPyro example [40]. The preliminary transformation of the posterior distribution with a trained autoguide is what is referred to in Refs. 39 and 40 as neural transport. NUTS is a user-friendly extension of Hamiltonian Monte Carlo (HMC) sampling that reduces the number of tuning parameters from 2 to 1 [41]. Instead of relying on random walks to explore the posterior distribution, HMC is a gradient-based Markov chain Monte Carlo method that converges significantly quicker than those that use random walks [41]. The sampling method described above was chosen because of the multimodal nature of the posterior distribution caused by the super-Gaussian mixture model, which makes it difficult for a sampler to efficiently explore the posterior distribution, even for a NUTS sampler on its own.

Implementing this sampling method is around eight lines of code using the code presented in Ref. 40, and to incorporate Eq. 7, the observed or synthetic data, and the priors into the code, we refer to the "Bayesian Regression Using NumPyro" NumPyro tutorial [42]. The autoguide was trained on 60,000 samples, and the NUTS sampler was run for four independent chains of 1000 warmup samples followed by 3000 samples. The NUTS sampler was run with a

PLEASE CITE THIS ARTICLE AS DOI: 10.1063/5.0281503

AIP Publishing

target acceptance probability of 0.99 and a step size of 0.1. While NUTS sampling on the untransformed posterior distribution was not effective with the presented method, techniques that can combine novel automatic differentiation methods with Hamiltonian Monte Carlo sampling may work with the presented method [43].

Once the samples of  $\vec{\theta}$  are generated, the corresponding  $f_k(v, \bar{\theta})$  is generated for each sample using Eqs. 4 and 5. When generating these sampled EVDFs, the lower and upper bounds of the electron velocity are ± 20,000 km/s and the resolution is 2 km/s. This was done to ensure the accuracy of the moments calculated from the sampled EVDFs. This resolution and the bounds were found to be appropriate for the temperature range considered in this work but should be adapted if the expected range of electron temperature is significantly different. For each sampled EVDF, the electron density, drift velocity along  $\vec{k}$ , effective temperature along  $\vec{k}$ , heat flux along  $\vec{k}$ , and excess kurtosis along  $\vec{k}$  are calculated through numerical integration of Eq. 9,

$$\begin{split} n_e &= \int f_k dv, u_{ek} = \frac{1}{n_e} \int v f_k dv, \\ T_{ek} &= \frac{m_e}{e n_e} \int c_e^2 f_k dv, q_{ek} = \frac{m_e}{2} \int c_e^3 f_k dv, \\ \Delta_{ek} &= \frac{1}{n_e} \left(\frac{m_e}{e T_{ek}}\right)^2 \int c_e^4 f_k dv - 3, \end{split} \tag{9}$$

where  $c = v - u_{ek}$ . After calculating the moments of each sampled EVDF, the posterior distribution for each moment of interest can then be constructed. The analysis focuses on the excess kurtosis instead of the kurtosis because of its presence in the heat flux transport equation [3] and because the excess kurtosis and the heat flux quantify the first-order deviation from a Maxwellian EVDF. Also, although the analysis focuses on quantifying the heat flux, the heat flux is related to the skewness of the EVDF,  $\beta$ , by  $\beta = \frac{2q_{ek}\sqrt{m_e}}{n_e(eT_{ek})^{3/2}}$ .

Next, this study considers the inferred parameters to be the mode of the posterior distributions. For a given posterior distribution of  $n_e$ ,  $u_{ek}$ ,  $T_{ek}$ ,  $q_{ek}$ , or  $\Delta_{ek}$ , the distribution is binned according to the Freedman-Diaconis rule, and the corresponding mode of the distribution is then found. To quantify the uncertainty of the inferred parameters, this work uses the 95% highest density intervals (HDIs) of the posterior distributions.

Figure 1 shows the key steps of the proposed method, including the steps used to determine the number of super-Gaussians used to analyze a given spectrum. To determine how many super-Gaussians to use to analyze a given spectrum, the method first starts by assuming that the EVDF is described by the sum of four super-Gaussians. The previously described sampling procedure is followed, except that the NUTS sampler is only run with one independent chain. If one of the four super-Gaussians has an average  $log_{10}(A_i)$  that is more than five lower than the maximum average  $log_{10}(A_i)$ , then the analysis concludes that the given spectrum is described by the sum of at most three super-Gaussians. That is, if  $log_{10}(A_1) = -6$ and  $\log_{10}(A_2) = 0$ , then  $f_1^{SG}(v)$  is considered negligible. This process is then repeated with three super-Gaussians, and so on, until none of the considered super-Gaussians are negligible. In addition, if the posterior distributions of  $n_e$ ,  $u_{ek}$ ,  $T_{ek}$ ,  $q_{ek}$ , or  $\Delta_{ek}$  are highly skewed, then the method reduces the number of super-Gaussians by one; this prevents the distribution with the smallest  $log_{10}(A_i)$  from trying to match noise in the tails of spectrum. This work defines highly skewed posterior distributions as those where the 95% HDI produces an uncertainty on one side of the mode that is at least five times greater than the uncertainty on the other side of the mode.

In the case where the ILTS spectrum is the average of thousands of laser shots in an unsteady discharge, then  $n_e \hat{f}_k$  in Eq. 2 should be replaced

PLEASE CITE THIS ARTICLE AS DOI: 10.1063/5.0281503

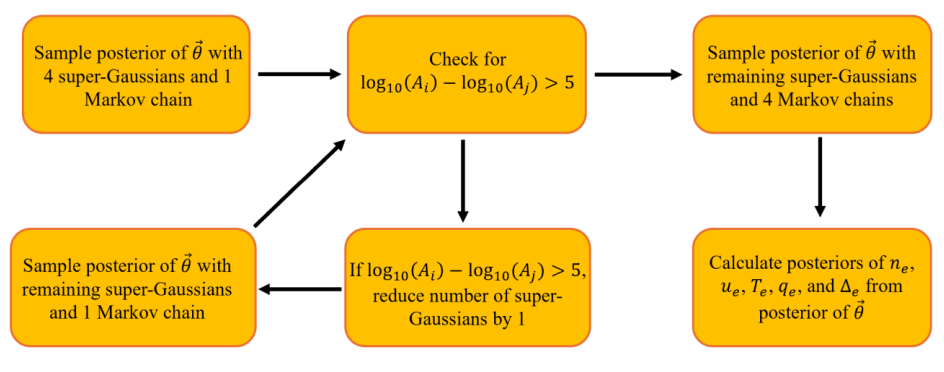


Figure 1. Schematic of key steps of the proposed Bayesian inference method

by  $\langle f_k \rangle$ , the time-averaged one-dimensional unnormalized EVDF along  $\vec{k}$ . In this case, the Bayesian inference will produce samples of  $\langle f_k \rangle$ , and for each sampled time-averaged unnormalized EVDF, the time-averaged electron density, current density along  $\vec{k}$ , pressure along  $\vec{k}$ , heat flux along  $\vec{k}$  and excess kurtosis along  $\vec{k}$  can be unambiguously calculated through numerical integration of Eq. 10,

$$\langle n_e \rangle = \int \langle f_k \rangle dv, \langle j_{ek} \rangle = e \int v \langle f_k \rangle dv,$$

$$\langle P_{ek} \rangle = m_e \int c_{\langle e \rangle}^2 \langle f_k \rangle dv,$$

$$\langle q_{ek} \rangle = \frac{m_e}{2} \int c_{\langle e \rangle}^3 \langle f_k \rangle dv,$$

$$\langle n_e \Delta_{ek} \rangle = \left( \frac{m_e \langle n_e \rangle}{\langle P_{ek} \rangle} \right)^2 \int c_{\langle e \rangle}^4 \langle f_k \rangle dv - 3 \langle n_e \rangle, (10)$$

where  $c_{\langle e \rangle} = v - \frac{\langle j_{ek} \rangle}{e\langle n_e \rangle}$ . In the presence of plasma oscillations, the interpretations of  $\langle q_{ek} \rangle$  and  $\langle n_e \Delta_{ek} \rangle$  are more nuanced as they can be nonzero even if the instantaneous EVDFs are Maxwellian. For example, if  $n_e$  and  $u_{ek}$  oscillate out of phase, then  $\langle q_{ek} \rangle$  can be nonzero even if  $q_{ek}$  is zero at every point in time, and if  $n_e$  and  $T_{ek}$  oscillate out of phase, then  $\langle n_e \Delta_{ek} \rangle$  can be nonzero even if  $\Delta_{ek}$  is zero at every point in time.

## 2.3. Generation of Synthetic ILTS Spectra

To evaluate the capabilities of the Bayesian inference methodology, the method needs to be tested against synthetic ILTS spectra. The first step in creating the synthetic spectra is defining the synthetic EVDFs. The four symmetric EVDFs this study considers are the 1D versions of the Maxwellian, Druyvesteyn, and Kappa distributions [44], defined as

$$\hat{f}^{M} = \frac{1}{\sqrt{\pi v_{th}^{2}}} \exp\left(-\frac{(v - v_{D})^{2}}{v_{th}^{2}}\right),\tag{11}$$

$$\hat{f}^{D} = \sqrt{\frac{\pi \Gamma(\frac{5}{4})}{6\Gamma(\frac{23}{4})^{3} v_{th}^{2}}} \operatorname{erfc}\left(\frac{2\Gamma(\frac{5}{4})(v-v_{D})^{2}}{3\Gamma(\frac{3}{4})v_{th}^{2}}\right),\tag{12}$$

$$\hat{f}^{\kappa} = \frac{\Gamma(\kappa + 3/2)}{\Gamma(\kappa + 1)} \frac{\left(1 + \frac{(\nu - \nu_D)^2}{\kappa \nu_{th}^2}\right)^{-(\kappa + 3/2)}}{\sqrt{\pi \kappa \nu_{th}^2}},$$
(13)

respectively, where  $v_{th} = \sqrt{\frac{2eT_e}{m_e}}$ . Next, from these symmetric EVDFs, skewed versions of Maxwellian, Druyvesteyn, and Kappa distributions are created with the transformation below,

$$\hat{f}^{skew} = \hat{f} \left( 1 - a \operatorname{erf} \left( \frac{2b(v - v_D)}{v_{th}^2} \right) \right), \tag{14}$$

where a and b are parameters that describe the skewness of the distributions. The 9 EVDFs that

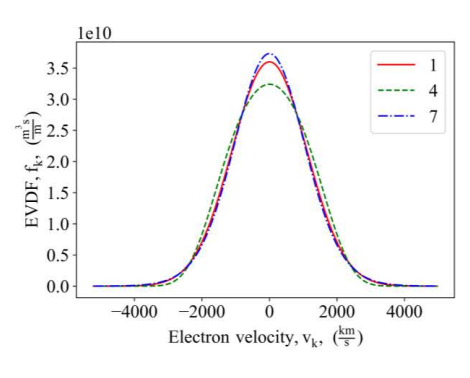


Figure 2. EVDFs corresponding to spectra 1, 4, and 7, representing Maxwellian, Druyvesteyn, and Kappa ( $\kappa = 10$ ) distributions, respectively.

this work tests the presented methodology against are described in Table 1 and plotted in Figs. 2-6. Table 1 includes five other distributions that are small variations of the EVDFs corresponding to spectra 1-9. Because a and b in Eq. 14 change the effective temperature and drift velocity of the EVDF, the values for  $v_D$  and  $T_e$  that we input in Eqs. 11-13 are those that ensure the corresponding values of  $u_e$  and  $T_e$  in Table 1.

Spectra 1-12 are meant to evaluate the methodology on EVDFs with different excess kurtosis and skewness. Spectrum 13 is meant to evaluate the methodology with different drift velocities. The impact of the drift velocity is to shift the rejection region within the EVDF, so Spectrum 13 effectively evaluates methodology when the rejection region is not at the peak of the EVDF. Spectrum 14 has the same EVDF as spectrum 7 but at a higher electron temperature, which evaluates the effect of a smaller rejection region with respect to the width of the EVDF. Lastly, spectra 15 and 16 have the same EVDF as spectrum 6 but at different temperatures and the same reference detection system, so spectra 15 and 16 are meant to evaluate the flexibility of the methodology on a

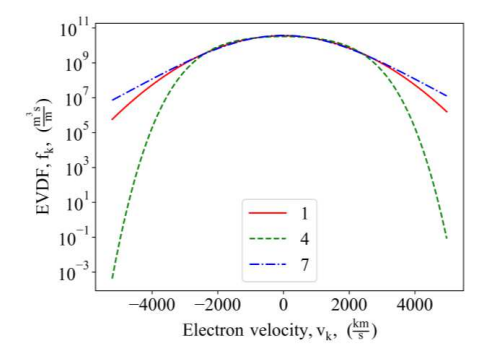


Figure 3. EVDFs corresponding to spectra 1, 4, and 7, representing Maxwellian, Druyvesteyn, and Kappa ( $\kappa = 10$ ) distributions, respectively. Yaxis is plotted on a log scale to show the tails of the EVDFs.

single detection system. It is important to note that for a given stray light filtering method and detection system, the effect of the rejection region is directly related to the effect of the spectral resolution.

To create a realistic synthetic ILTS spectra from a synthetic EVDF, it is necessary to use a realistic rejection region, instrument function,

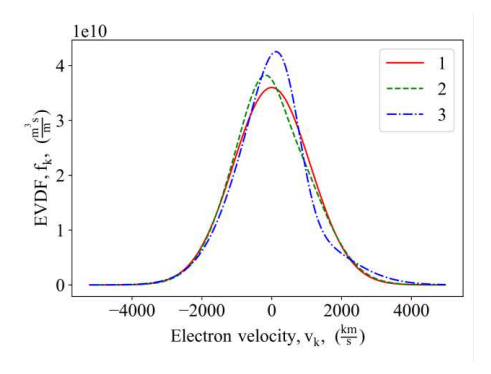


Figure 4. EVDFs corresponding to spectra 1, 2, and 3, representing a Maxwellian distribution and its skewed counterparts.



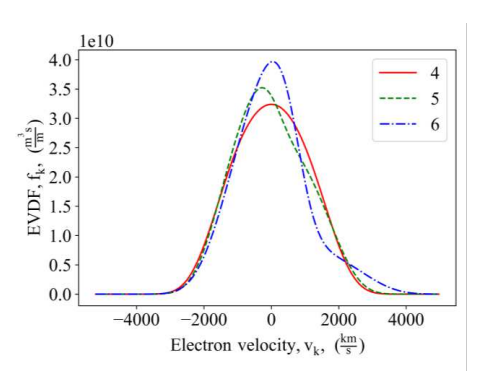


Figure 5. EVDFs corresponding to spectra 4, 5, and 6, representing a Druyvesteyn distribution and its skewed counterparts.

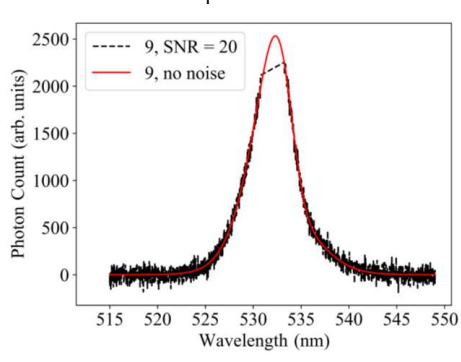


Figure 7. Synthetic ILTS spectrum of spectrum 9 on detection system B and an SNR of 20. Also shown is the corresponding synthetic spectrum with no noise and no rejection region.

and wavelength array. The choices of rejection region and instrument function are based on a reference detection system from a combination of low-temperature ILTS diagnostics that use volume Bragg grating based notch filters (VBG-NFs) and an ICCD [45, 46]. The reference rejection region will have a width of 2.5 nm, and the reference instrument function will be a Gaussian distribution centered at 532 nm with a standard deviation of 0.5 nm. The reference wavelength array will have 1024 elements and

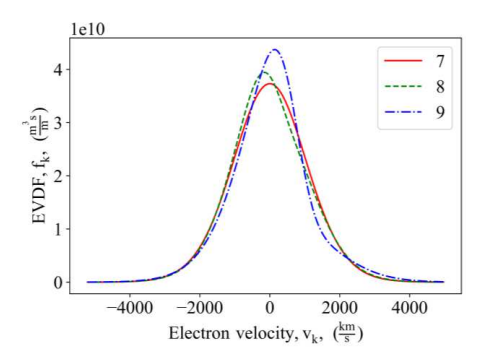


Figure 6. EVDFs corresponding to spectra 7, 8, and 9, representing a Kappa distribution ( $\kappa = 10$ ) and its skewed counterparts.

will be centered at 532 nm with a range of 17 nm. This reference detection system is denoted as detection system A.

In addition, for an accurate analysis, different EVDFs may require a higher spectral resolution or the same spectra resolution with a wider wavelength range. Because of this, the analysis will also consider different reference detection systems to illustrate the benefit of using different detection systems or acquisition strategies to analyze different EVDFs. Detection system B has the same rejection region, instrument function, and spectral resolution as detection system A, but its wavelength range is 34 nm. Detection system B is representative of acquiring two different spectra with the same detection system but with each spectrum being centered at different wavelengths. Detection system C has half the rejection region of system A, an instrument function with half the standard deviation of that of system A, twice the spectral resolution of system A, and the same spectral range as system A. Detection system C is representative of using a higher resolution grating than that used for system A, but acquiring two different spectra to achieve the same spectral range. Detection system D has the same rejection region, instrument function, and spectral resolution as

This is the author's peer reviewed, accepted manuscript. However, the online version of record will be different from this version once it has been copyedited and typeset

PLEASE CITE THIS ARTICLE AS DOI: 10.1063/5.0281503

Spectrum	Distribution	Detection	Number	a	b	$u_e$	$T_e$	$q_e$	$\Delta_e$
#	type	system	of $f_i^{SG}$		0	(km/s)	(eV)	(W/cm <sup>2</sup> )	
1	Maxwellian	A	1	0	0	0	7	0	0
2	Maxwellian	В	2	0.2	1	0	7	0.525	0.045
3	Maxwellian	В	3	0.7	3	0	7	2.034	1.201
4	Druyvesteyn	В	2	0	0	0	7	0	-0.532
5	Druyvesteyn	D	2	0.2	1	0	7	0.779	-0.483
6	Druyvesteyn	D	4	0.7	3	0	7	3.265	0.716
7	Kappa = 10	D	2	0	0	0	7	0	0.333
8	Kappa = 10	В	2	0.2	1	0	7	0.403	0.379
9	Kappa = 10	D	3	0.7	3	0	7	1.448	1.575
10	Kappa = 30	D	2	0	0	0	7	0	0.103
11	Kappa = 20	D	2	0	0	0	7	0	0.158
12	Kappa = 5	D	2	0	0	0	7	0	0.749
13	Kappa = 10	F	2	0	0	0	25	0	0.333
14	Kappa = 10	E	3	0.7	3	400	7	1.448	1.575
15	Druyvesteyn	D	3	0.7	3	0	1.03	0.183	0.716
16	Druyvesteyn	D	4	0.7	3	0	10.95	6.391	0.716

Table 1. Properties of the 16 synthetic spectra, including the underlying type of symmetric EVDF, the values of a and b used in Eq. 14, and the corresponding values of the electron drift velocity, effective temperature, heat flux, and excess kurtosis. For all cases, the electron density was  $10^{17} m^{-3}$ . Also shown are the detection systems that were necessary to accurately analyze the spectra and the number of super-Gaussians required to describe the spectra. For the Kappa distributions, the value of  $\kappa$  is denoted.

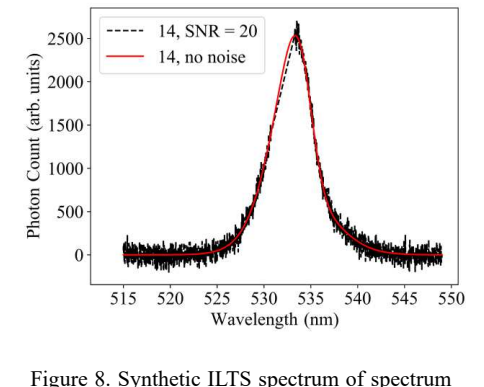
system C but has 1.5 times the spectral range of system A. Detection system E has the same rejection region, instrument function, and spectral resolution as system C, but has the same spectral range as system B, and detection system F has twice the spectral range of detection system E and is the same otherwise.

Next, since  $\sigma_T$  is constant between the generation of the synthetic spectra and the application of the Bayesian methodology,  $\sigma_T$  was set to 1 in the implementation of the methodology. An incident wavelength of 532 nm, a scattering angle of 90°, and a calibration constant of C=0.5 are also assumed. From Eqs. 1-3, the synthetic ILTS spectra for a given synthetic EVDF is then constructed. The last step to generate the realistic ILTS spectra is to add

Gaussian noise to the spectra, which is done with an SNR of 20 decibels. These SNR and noise profiles are representative of real ILTS measurements on low-temperature plasmas. Spectra 9 and 14 are shown in Figs. 7 and 8 to show how the drift velocity changes where the rejection region is with respect to the shape of the spectrum.

Lastly, to evaluate the Bayesian inference methodology, an example prior distribution for the LRS calibration constant needs to be defined. The example prior distribution used in this work is a normal distribution centered at  $\mathcal{C}=0.5$  with a standard deviation of 0.025. The standard deviation is chosen to represent the 10% uncertainty in the Raman scattering cross section of  $N_2$  that typically dominates the uncertainty in

PLEASE CITE THIS ARTICLE AS DOI: 10.1063/5.0281503



14 on detection system B and an SNR of 20. Also shown is the corresponding synthetic spectrum with no noise and no rejection region. the calibration constant obtained from LRS. In terms of processing time on a standard laptop, if using the sum of four super-Gaussians with the high spectral resolution of detection system D, analysis of a single spectrum takes around 15 minutes, and it takes around 3 minutes for the sum of two super-Gaussians with detection

## 3. Results and Discussion

system B.

In this section, the Bayesian inference method is evaluated on the synthetic spectra shown in Section 2.3 regarding the method's accuracy and precision. The evaluation primarily focuses on the method's accuracy and precision of inferences of the heat flux and excess kurtosis. It is found that the methodology performs better on certain spectra, and this section also compares the proposed method to a simplified method that treats the EVDFs as sums of Gaussians. The method is considered to have adequate accuracy when the 95% HDIs of the first five moments of the EVDF contain the true values listed in Table 1. An important general finding is that for all the spectra considered, the proposed method is adequately accurate for inferences of the electron density, drift velocity, and heat flux. In addition,

because the heat flux and excess kurtosis are deviations from Maxwellian EVDFs and thus have true values at or close to zero, it is not always appropriate to assess the method's precision with relative uncertainty. Instead of focusing on relative uncertainty when the inferred values are close to zero, the analysis will relate the bounds of the 95% HDI to the minimum detectable values of the heat flux and excess kurtosis with ILTS.

## 3.1. Evaluation of the Proposed Method

At an SNR of 20, the minimum detectable values of the electron heat flux and excess kurtosis can be approximated by the results in Table 2 of the analysis on spectra 1 and 4, respectively. From the 95% HDI of the excess kurtosis for spectrum 1, the minimum detectable excess kurtosis at 20 SNR is approximately ± 0.07. From the 95% HDI of the heat flux for spectrum 4, the minimum detectable excess kurtosis at 20 SNR is approximately ± 0.04 W/cm<sup>2</sup>. In general, it is more useful to consider the minimum detectable skewness, which in this case would be ± 0.006. Additionally, whenever the true value of a property is 0 or less than the minimum detectable value, it is found that the 95% HDI includes 0. The analysis can then

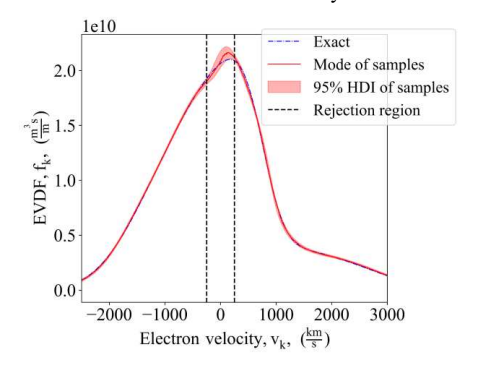


Figure 9. Inferred EVDF from spectrum 6 using the presented method. Also shown is the corresponding exact EVDF.

#	$n_e  (10^{16}  \mathrm{m}^{-3})$	u <sub>e</sub> (km/s)	$T_e$ (eV)	$q_e  (\text{mW/mm}^2)$	$10\Delta_e$
1	9.8 + 0.9 / - 0.6	1.2 + 8.4 / - 7	6.96 + 0.18 / - 0.13	0	-0.46 + 0.75 / - 0.70
2	9.9 + 0.8 / - 0.6	2.5 + 7.8 / - 7.7	7.00 + 0.15 / - 0.09	$4.89 \pm 1.35$	0.74 + 0.80 / - $0.68$
3	10.0 + 0.9 / - 0.7	-3.1 + 8.8 / - 9.6	6.78 + 0.27 / - 0.14	18.18 + 3.89 / - 3.06	10.19 + 1.82 / - 1.30
4	$9.9 \pm 0.7$	-1.6 + 6.4 / - 5.9	$7.06 \pm 0.10$	-0.01 + 0.42 / - 0.35	-5.26 + 0.34 / - 0.38
5	10.3 + 0.5 / - 0.9	-3.1 + 6.0 / - 6.8	7.01 + 0.07 / - 0.10	7.11 + 1.06 / - 0.83	-4.97 + 0.33 / - 0.25
6	9.8 + 0.9 / - 0.6	-2.4 + 9.1 / - 9.5	6.96 + 0.19 / - 0.13	30.34 + 4.47 / - 3.12	6.60 + 1.17 / - 0.92
7	10.1 + 0.3 / - 0.6	1.4 + 4.9 / - 4.1	6.87 + 0.12 / - 0.11	$-0.19 \pm 0.50$	2.12 + 0.76 / - 0.64
8	9.9 + 0.8 / - 0.7	2.7 + 7.3 / - 6.6	6.92 + 0.13 / - 0.12	3.85 + 1.02 / - 1.15	1.84 + 0.80 / - 0.90
9	9.9 + 0.6 / - 0.5	-8.5 + 10.4 / - 10.3	6.88 + 0.32 / - 0.21	11.37 + 4.68 / - 3.26	14.09 + 3.27 / - 2.19
10	10.1 + 0.4 / - 0.6	2.9 + 4.9 / - 4.8	7.04 + 0.10 / - 0.09	0.15 + 0.56 / - $0.32$	1.10 + 0.47 / - 0.36
11	$10.0 \pm 0.6$	-2.4 + 5.5 / - 5.9	7.06 + 0.12 / - 0.15	-0.38 + 0.60 / - 0.78	1.53 + 0.91 / - 0.71
12	$10.0 \pm 0.6$	-4.5 + 5.0 / - 5.1	6.74 + 0.16 / - 0.14	-0.16 + 0.58 / - 0.68	4.21 + 1.16 / - 1.11
13	9.8 + 0.8 / - 0.6	3.9 + 12.6 / - 15.7	24.8 + 0.6 / - 0.5	0.54 + 7.74 / - 11.62	2.93 + 1.63 / - 0.94
14	9.8 + 0.6 / - 0.4	401 + 10 / - 12	6.81 + 0.22 / - 0.15	14.23 + 4.37 / - 5.95	12.29 + 1.94 / - 1.29
15	9.7 + 0.8 / - 0.4	-0.3 + 3.3 / - 2.5	$1.02 + \pm 0.02$	1.83 + 0.26 / - 0.18	5.79 + 1.42 / - 0.90
16	9.9 + 0.9 / - 0.7	-0.8 + 12.6 / - 13.7	$11.0 \pm 0.3$	61.93 + 10.60 / - 7.78	6.93 + 1.28 / - 1.20

Table 2. Inferred moments of the EVDF from the synthetic spectra using the presented Bayesian inference method. Inferences are presented as the mode of the posterior distributions and uncertainty bounds based on the 95% HDI of the posterior distributions. Values are bolded when the true value in Table 1 is not within the 95% HDI.

consider the accuracy and precision of the proposed method for distributions with magnitudes of heat flux or excess kurtosis above these minimum values.

Regarding the accuracy of the proposed method on skewed Maxwellians, Table 2 shows that the proposed method achieves adequate accuracy for all properties, and Table 3 shows that the proposed method can achieve a relative error of electron heat flux measurements of less than 11%. In addition, when the true value of the excess kurtosis is above the minimum detectable value, as in spectrum 3, the method achieves a relative error of the excess kurtosis of 15.2%. This demonstrates that if the true values of the excess kurtosis and heat flux are above the minimum detectable values for a given SNR, then ILTS can accurately infer the excess kurtosis and heat flux for skewed Maxwellians. In terms of the

precision of such inferences, the relative uncertainty of the inferred heat flux and excess kurtosis decreases as the deviation from

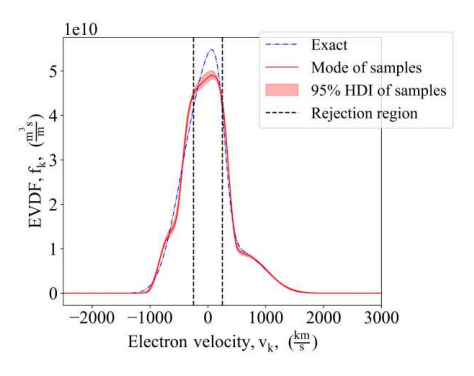


Figure 10. Inferred EVDF from spectrum 15 using the presented method. Also shown is the corresponding exact EVDF.

PLEASE CITE THIS ARTICLE AS DOI: 10.1063/5.0281503

10<sup>10</sup>

Figure 11. Inferred EVDF from spectrum 6 using the presented method. Also shown is the corresponding exact EVDF. Y-axis is plotted on a log scale to show the tails of the EVDFs.

Maxwellian EVDFs increases, as shown in Table 4. Relative uncertainties for the electron heat flux are between 15% and 30%, and when the excess kurtosis is above the minimum detectable value, the relative uncertainty is around 15%.

As for the accuracy of the proposed method on Druyvesteyn distributions and their skewed counterparts, Table 2 shows that the proposed method achieves adequate accuracy for all properties. From Table 3, the relative errors in heat flux and excess kurtosis are all below 10% when  $T_e = 7$  eV. From Table 4, all relative uncertainties are below 20%, with the excess kurtosis having relative uncertainties below 10% when the heat flux is low and  $T_e = 7$  eV. Additionally, the electron temperatures of spectra 15 and 16 represent approximate lower and upper limits of electron temperature, respectively, at which the corresponding shape of the EVDF can be accurately analyzed with the proposed method with detection system D. The increased relative error and relative uncertainty in the excess kurtosis for spectrum 15 are caused by the increased effect of the rejection region. The increased effect of the rejection region can also be visualized in the inferred EVDFs in Figs. 9 and

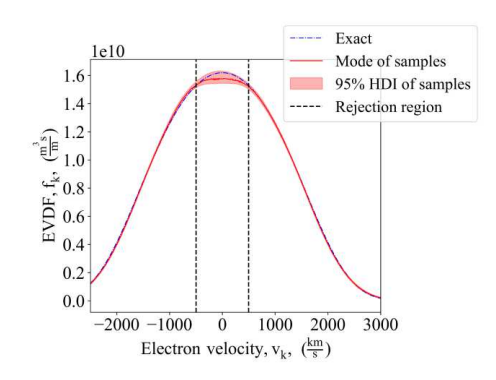


Figure 12. Inferred EVDF from spectrum 4 using the presented method. Also shown is the corresponding exact EVDF.

10 and is seen to decrease the accuracy of the inferred EVDF both within and outside the rejection region. In this case, the lower limit for the electron temperature corresponded to when one of the super-Gaussians reached the lower limit of  $\Delta v_i$  of 420 km/s. While the analysis of spectrum 16 has a similar accuracy and precision as that on spectrum 6, at even higher electron temperatures, inaccuracies and imprecision are

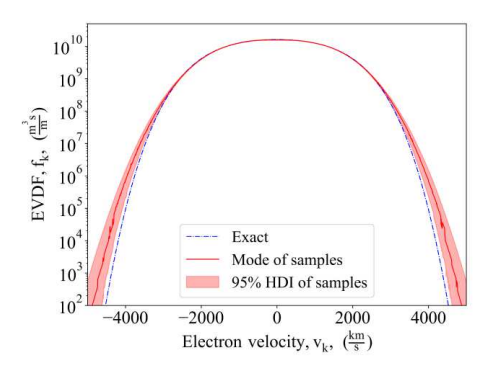


Figure 13. Inferred EVDF from spectrum 4 using the presented method. Also shown is the corresponding exact EVDF. Y-axis is plotted on a log scale to show the tails of the EVDFs.

PLEASE CITE THIS ARTICLE AS DOI: 10.1063/5.0281503

#	Relative error in $q_e$ (%)	Relative error in $\Delta_e$ (%)
2	6.9	64.4
3	10.6	15.2
4	-	1.1
5	9.7	2.9
6	7.1	7.8
7	-	36.3
8	4.5	51.5
9	21.5	10.5
10	-	6.8
11	-	3.16
12	-	43.8
13	-	12.0
14	1.73	22.0
15	0	19.1
16	3.1	3.2

Table 3. Relative errors of the heat flux and excess kurtosis from the presented method for all the spectra with either a nonzero true heat flux or true excess kurtosis. When the true value of the heat flux is zero, the relative error is not shown. Relative error is based on the mode of the posterior distribution with respect to the true value.

caused by a smaller proportion of the EVDF being included in the analysis.

In general, it is found that the inferences of electron heat flux and excess kurtosis are more precise for Druyvesteyn EVDFs and their skewed counterparts than for skewed Maxwellian EVDFs. This is likely due to the depleted tails of Druyvesteyn distributions. The tails of the EVDFs are generally below the noise floor of ILTS spectra, so with depleted tails, more information is located above the noise floor. Since EVDFs with depleted tails are more common in low-temperature plasmas, this indicates that ILTS is well suited to infer the

#	Relative uncertainty in $q_e$ (%)	Relative uncertainty in $\Delta_e$ (%)
2	± 27.6	+ 108.1 / - 91.9
3	+ 21.4 / - 16.8	+ 17.9 / - 12.8
4	-	+ 6.5 / - 7.2
5	+ 14.9 / - 11.7	+ 6.6 / - 5.0
6	+ 14.7 / -10.3	+ 17.7 / - 13.9
7	-	+ 35.8 / - 30.2
8	+ 26.5 / - 29.9	+ 43.5 / - 48.9
9	+ 41.2 / - 28.7	+ 23.2 / - 15.5
10	-	+ 42.7 / - 32.7
11	-	+ 40.5 / - 53.6
12	-	27.6 / - 26.4
13	-	+ 55.6 / - 32.1
14	+ 30.7 / - 41.8	+ 15.8 / - 10.5
15	+ 14.2 / - 9.8	+ 24.5 / - 15.5
16	+ 17.1 / - 12.6	+ 18.5 / - 17.3

Table 4. Relative uncertainties of the heat flux and excess kurtosis from the presented method for all the spectra with either a nonzero true heat flux or true excess kurtosis. When the true value of the heat flux is zero, the relative uncertainty is not shown. Relative error is based on the uncertainty bounds from the 95% HDI of the posterior relative to the mode of the posterior distribution.

higher-order moments of EVDFs in low-temperature plasmas. However, non-Maxwellian EVDFs in low-temperature plasma can have sudden depletion of the tails after the threshold energy of either an inelastic collision [47] or of the sheath potential [4, 8], and if this threshold energy occurs below the noise floor of ILTS, then the proposed method would not enable ILTS to detect such EVDFs. In addition, for the case of spectrum 6, the accuracy of the inferred EVDF below the noise floor is surprisingly high, as shown in Fig. 11, which is further evidence that Druyvesteyn EVDFs and their skewed counterparts contain a significant amount of

PLEASE CITE THIS ARTICLE AS DOI: 10.1063/5.0281503

information above the noise floor. Lastly, the accurate inference for Druyvesteyn distributions is also seen in Figs. 12 and 13.

Similar reasoning explains the effects of the spectral resolution, since if the rejection region takes up a larger proportion of the spectrum, then less information is available, which decreases the accuracy and precision. For a constant detection system, the effect of the rejection region becomes greater at lower electron temperatures, such that each type of EVDF has a lower limit for the electron temperature at which a detection system can be used to accurately analyze that type of distribution. In addition, because of the finite bandwidth of VBG-NFs, each type of EVDF has a fundamental lower limit for the electron temperature for which ILTS can be accurately used to analyze that type of EVDF. The Maxwellian and Druyvesteyn distributions analyzed in this work are above these lower limits.

The effect of relative spectral range has competing effects. For a given detection system, as electron temperature increases, the tails of the EVDF are truncated, which decreases the amount of information in the spectrum, but the effect of

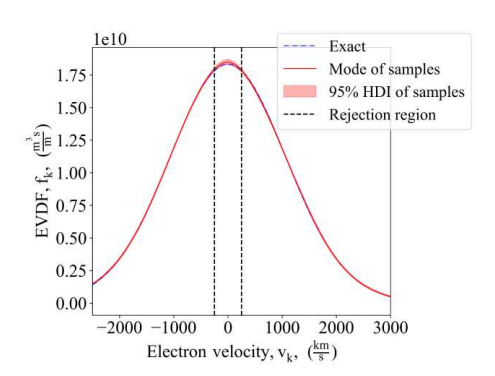


Figure 14. Inferred EVDF from spectrum 11 using the presented method. Also shown is the corresponding exact EVDF.

the rejection region decreases, which increases the amount of information available. However, for sufficiently high electron temperatures, the increased benefit of a smaller rejection region is negligible, and the increasing effect of truncated tails will produce inaccurate and imprecise inferences. This may explain why spectrum 14 does not experience a noticeable decrease in accuracy or precision with respect to spectrum 6, even though some information above the noise floor in the tails of the EVDF of spectrum 16 is lost when using detection system D.

Regarding its efficacy on distributions, the method does not accurately capture the electron temperature or the excess kurtosis if the skewness and temperature are too low, as in spectra 7, 8, and 12. Even for these inaccurate cases, the proposed method is adequately accurate for the inferences of the electron density, drift velocity, and heat flux. The relative error in the excess kurtosis decreases to around 10% for sufficiently high heat flux, sufficiently low excess kurtosis, and higher electron temperature, as shown by spectra 9, 10, 11, and 13, respectively. The inferred EVDF for spectrum 11 is shown in Figs. 14 and 15, as it is

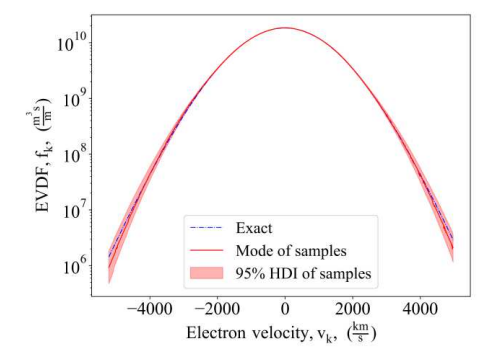
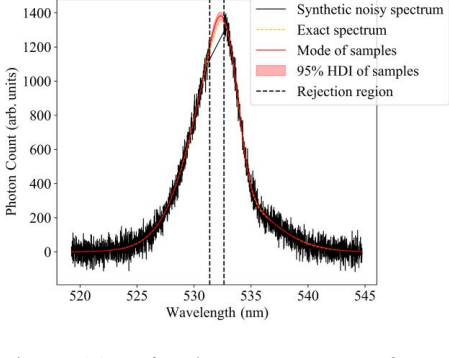


Figure 15. Inferred EVDF from spectrum 11 using the presented method. Also shown is the corresponding exact EVDF. Y-axis is plotted on a log scale to show the tails of the EVDFs.

PLEASE CITE THIS ARTICLE AS DOI: 10.1063/5.0281503



Synthetic noisy spectrum

Figure 16. Inferred ILTS spectrum from spectrum 9 using the presented method. Also shown are the corresponding exact spectrum and the corresponding synthetic noisy spectrum on detection system D with an SNR of 20.

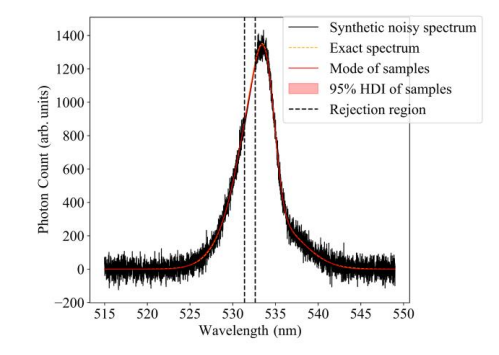


Figure 17. Inferred ILTS spectrum from spectrum 14 using the presented method. Also shown are the corresponding exact spectrum and the corresponding synthetic noisy spectrum on detection system E with an SNR of 20.

#	$\vec{\theta}_1\left(-,\frac{Mm}{s},\frac{Mm}{s},-\right)$	$\vec{\theta}_2\left(-,\frac{Mm}{s},\frac{Mm}{s},-\right)$	$\vec{\theta}_3\left(-,\frac{Mm}{s},\frac{Mm}{s},-\right)$	$\vec{\theta}_4\left(-,\frac{Mm}{s},\frac{Mm}{s},-\right)$
2	0.12, 1.28, -0.10, 1.85	-0.09, 1.91, 0.12, 2.42	-	-
3	0.16, 1.03, -0.29, 1.58	0.00, 0.50, 0.36, 2.66	-0.51, 2.60, 0.30, 2.93	-
4	0.23, 1.67, 0.01, 2.48	-0.48, 2.20, -0.04, 5.23	-	-
5	0.00, 2.06, 0.10, 3.71	-0.06, 1.21, -0.20, 2.17	-	-
6	-0.14, 1.04, -0.16, 3.41	-0.31, 1.45, -0.63, 3.58	-0.33, 0.60, 0.28, 3.14	-0.44, 2.34, 0.58, 3.23
9	0.03, 0.57, 0.32, 2.61	0.00, 0.92, -0.41, 1.58	-0.46, 2.39, 0.26, 2.46	-
10	0.27, 1.56, 0.01, 1.96	-1.20, 1.22, -0.26, 3.89	-	-
11	0.25, 1.53, -0.01, 1.85	-0.90, 1.52, 0.11, 3.77	-	-

Table 5. Means of the posterior distributions of the super-Gaussian model parameters,  $\vec{\theta}$ , as defined in Section 2.1. Results were obtained from the synthetic spectra using the proposed method. For readability,  $\vec{\theta}$  is split into  $\vec{\theta}_1$ ,  $\vec{\theta}_2$ ,  $\vec{\theta}_3$ , and  $\vec{\theta}_4$ , corresponding to the individual super-Gaussians. As displayed in the table,  $\vec{\theta}_i = \left[\log_{10}(A_i), \Delta v_i, v_{D,i}, b_i\right]$ .  $\vec{\theta}$  is only presented for spectra corresponding to unique non-Maxwellian EVDFs and for spectra for which the proposed method is adequately accurate.

This is the author's peer reviewed, accepted manuscript. However, the online version of record will be different from this version once it has been copyedited and typeset. PLEASE CITE THIS ARTICLE AS DOI: 10.1063/5.0281503

#	$n_e (10^{16} \mathrm{m}^{-3})$	u <sub>e</sub> (km/s)	$T_e$ (eV)	q <sub>e</sub> (mW/mm <sup>2</sup> )	$10\Delta_e$
1	10.0 + 0.7 / - 0.8	0.7 + 8.3 / - 8.6	6.98 + 0.13 / - 0.12	0	0
2	$10.0 \pm 0.7$	-3.9 + 7.9 / - 6.5	7.03 + 0.09 / - 0.10	4.35 + 1.27 / - 1.14	0.72 + 0.39 / - $0.38$
3	10.2 + 1.0 / - 0.8	-3.6 + 10.9 / - 9.5	7.19 + 0.22 / - 0.19	20.15 + 4.97 / - 3.91	16.83 + 1.10 / - 0.91
4	9.9 + 1.0 / - 0.7	3.7 + 8.4 / - 6.9	7.30 + 0.07 / - 0.08	-0.17 + 1.14 / - 1.06	-4.17 + 0.22 / - 0.27
5	$10.0 \pm 0.7$	-0.9 + 7.8 / - 0.7	7.30 + 0.07 / - 0.08	9.05 + 1.37 / - 1.07	-3.42 + 0.22 / - 0.19
6	9.6 + 0.6 / - 0.5	4.9 + 9.0 / - 9.3	7.02 + 0.15 / - 0.14	31.86 + 2.84 / - 4.23	7.58 + 0.78 / - 1.13
7	9.9 + 0.8 / - 0.7	0.3 + 7.0 / - 8.6	6.94 + 0.15 / - 0.13	-0.7 + 1.33 / - 1.50	2.74 + 0.96 / - 0.74
8	9.8 + 1.0 / - 0.6	4.2 + 7.9 / - 7.8	6.92 + 0.14 / - 0.12	5.38 + 2.29 / - 1.37	2.90 + 0.92 / - 0,77
9	10.0 + 0.8 / - 0.6	-1.4 + 11.6 / - 10.5	$7.37 \pm 0.21$	12.51 + 4.08 / - 3.92	18.26 + 1.23 / - 1.14
10	9.9 + 0.7 / - 0.5	-7.7 + 6.3 / - 5.2	6.97 + 0.08 / - 0.10	-0.25 + 0.44 / - 0.49	0.42 + 0.35 / - 0.24
11	$10.0 \pm 0.6$	4.5 + 5.1 / - 6.0	6.92 + 0.08 / - 0.10	0.10 + 0.46 / - $0.47$	0.51 + 0.39 / - 0.21
12	9.9 + 0.9 / - 0.6	-7.3 + 8.0 / - 7.8	6.82 + 0.19 / - 0.14	-0.64 + 1.27 / - 1.84	4.75 + 1.44 / - 1.00
13	10.0 + 0.6 / - 0.8	2.5 + 11.3 / - 9.7	25.1 + 0.3 / - 0.4	3.04 + 8.15 / - 8.35	3.48 + 0.83 / - 0.76
14	10.0 + 0.6 / - 0.7	389 + 11 / - 9	$7.04 \pm 0.19$	9.42 + 4.17 / - 2.74	16.69 + 1.25 / - 1.03
15	$9.9 \pm 0.6$	$1.1 \pm 2.7$	$1.09\pm0.02$	2.07 + 0.23 / - 0.16	8.69 + 0.60 / - 0.50
16	$9.8 \pm 0.6$	2.2 + 14.4 / - 11.5	11.2 + 0.3 / - 0.2	68.46 + 9.49 / - 7.85	8.51 + 0.95 / - 1.05

Table 6. Inferred moments of the EVDF from the synthetic spectra using the simplified Bayesian inference method. Inferences are presented as the mode of the posterior distributions and uncertainty bounds based on the 95% HDI of the posterior distributions. Values are bolded when the true value in Table 1 is not within the 95% HDI.

the spectrum with the lowest relative uncertainty for the excess kurtosis among all the EVDFs with Kappa distributions. However, even for the accurate cases of spectra 9, 10, 11, and 13, the relative uncertainties for the heat flux and excess kurtosis are higher than for the analysis of Maxwellian distributions. Additionally, the proposed method is not adequately accurate for spectrum 14 for inferences of electron temperature and excess kurtosis; this inaccuracy is due to the drift velocity, which effectively shifts the location of the rejection region along the EVDF, suggesting that different locations of the EVDF contain more important information than others. The importance of the location of the rejection region is also relevant to the effect of poorly subtracted emission spectra when collecting ILTS data, as poorly subtracted

emission spectra would lead to additional rejection regions.

Figures 16 and 17 compare the inferred ILTS spectra from spectra 9 and 14, respectively, to their corresponding synthetic spectra. The inferred spectra are reconstructed from the inferred EVDFs and the instrument function. Interestingly, the inferred spectrum for spectrum 9 deviates from the exact spectrum within the rejection region, which is not the case for spectrum 14. Although the difference between synthetic spectra 9 and 14 is predominantly the location of the rejection region relative to the shape of the EVDF, the reduced accuracy of the inference on spectrum 14 is not caused by inaccuracies within the rejection region. Instead, the location of the rejection region in spectrum 14

PLEASE CITE THIS ARTICLE AS DOI: 10.1063/5.0281503

## AIP Publishing

results in reduced accuracy of the inferred spectrum in the tails of the spectrum.

The worse performance of the proposed method on Kappa distributions is for the same reason that the method performs well for Druyvesteyn distributions. For distributions with positive excess kurtosis, more information is in the tails below the noise floor. This explains the improved performance of the method for sufficiently high heat flux, sufficiently low excess kurtosis, and higher electron temperature. If the skewness is high enough, as in spectrum 9, then there is sufficient information above the noise floor for the proposed method to be adequately accurate. For higher electron temperatures, assuming that the same proportion of the EVDF is analyzed but with a constant width of the rejection region, then the effect of the rejection region will reduce, and the same amount information is lost in the tails. The adequate accuracy of the analysis of spectrum 13 indicates that a smaller rejection region can improve the performance of the proposed method on Kappa distributions. However, in general, careful consideration of the detection system and expected SNR, drift velocity, and temperature is necessary to determine whether ILTS can be used to accurately analyze a specific EVDF with low skewness and positive excess kurtosis. In fact, similar careful consideration of the detection system and acquisition strategy is necessary to accurately measure higher-order moments from EVDFs with negative excess kurtosis. This can be seen in Table 1, since several spectra required analysis with reduced rejection regions, such as detection systems D, E, and F.

The parameters of the inferred super-Gaussians are shown in Table 5. Unsurprisingly, all the super-Gaussian components inferred for the Druyvesteyn distribution and its skewed counterparts have depleted tails. On the other hand, there is always one super-Gaussian component with depleted tails for the inferences

on the Kappa distribution and its skewed counterparts. For the high skew cases of spectra 3, 6, and 9, the super-Gaussian component with the lowest density has the highest temperature by more than factor of 2.

## 3.2. Comparison with Simplified Method

For each spectrum, the simplified methodology was implemented with the same detection system and number of distributions as the proposed methodology, but each EVDF was the sum of Gaussians instead of super-Gaussians. As shown in Table 6, the simplified method has inadequate accuracy for the excess kurtosis for more spectra than the proposed method, and in some cases, inaccuracies are introduced for the drift velocities and heat flux. In particular, the simplified method is not adequately accurate for Druyvesteyn EVDFs and their skewed counterparts and for the high-skew EVDFs of spectra 3 and 9. Meanwhile, spectra 7 and 8 are the only spectra for which the proposed method does not have adequate accuracy but for which the simplified method does have adequate accuracy. Because the simplified method is only better than the proposed method for a limited range of Kappa distributions, the simplified method is not a general improvement to the proposed method for Kappa distributions. In addition, the simplified method generally has smaller uncertainty bounds than the proposed method, which can be explained by the fact that the proposed method considers more shapes of the EVDF.

Due to the inaccuracies of the simplified method, it is useful to consider the general impact of inaccuracies in the inferences of the heat flux and excess kurtosis. For the joint posterior distribution shown in Fig. 18, the drift velocity is most strongly correlated with the heat flux, and the temperature is most strongly correlated with the excess kurtosis. These correlations quantify how accounting for non-Maxwellian features is

PLEASE CITE THIS ARTICLE AS DOI: 10.1063/5.0281503

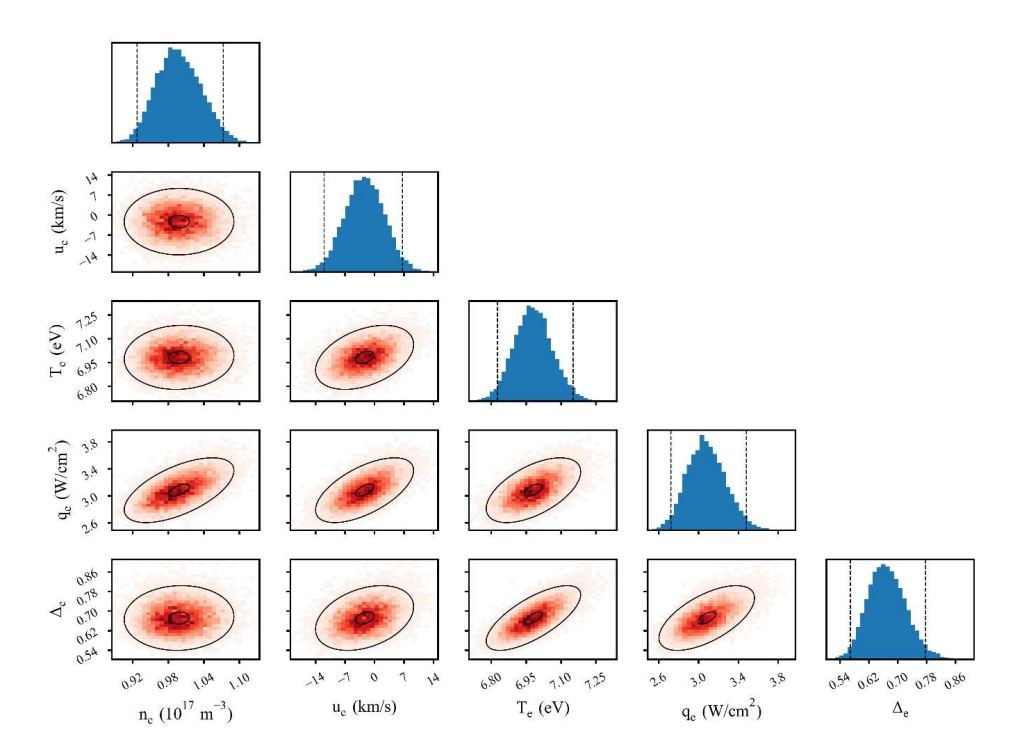


Figure 18. Marginal and joint posterior distributions of the electron density, drift velocity, temperature, heat flux and excess kurtosis. In the marginal distributions, the 95% HDIs are denoted with the vertical dashed lines. In the joint distributions, the Mahalanobis contours containing the most probable 10% and 95% of the distribution are shown. Posterior distributions are from the proposed method on spectrum 6.

necessary to accurately infer the drift velocity and temperature. This is observed in Table 2, as the proposed methodology is adequately accurate for both the heat flux and drift velocity for all cases, but whenever the proposed method is inadequate for the excess kurtosis, the relative error in the temperature inference increases.

## 4. Conclusion

In conclusion, this study has found that the presented Bayesian inference method can accurately expand the capabilities of ILTS to direct measurements of the electron heat flux and excess kurtosis. Specifically, for all the synthetic

spectra considered, the presented method is adequately accurate for inferences of the heat flux with uncertainties ranging from around 40% to as low as around 10%. Notably, the method can accurately infer the excess kurtosis of Druyvesteyn distributions with an uncertainty of around 5%. In addition, the presented method performs favorably compared to a simplified method that only uses Gaussian distributions instead of super-Gaussians. However, the presented method does not accurately infer the excess kurtosis of certain Kappa distributions. To accurately infer the excess kurtosis of a wide variety of EVDFs with positive excess kurtosis

PLEASE CITE THIS ARTICLE AS DOI: 10.1063/5.0281503

and low skewness, high SNR measurements are needed in order that a significant portion of the tails are above the noise floor.

Future work should include implementing this method with actual measurements, which would enable high-fidelity validation of simulations that account for non-Maxwellian EVDFs. To do such measurements, it is necessary to carefully select the detection system and acquisition strategy to mitigate the effects of spectral resolution and spectral range. In addition, inferences of higher-order moments will be more affected by improper subtraction of stray light sources when constructing ILTS spectra. Lastly, although the synthetic spectra were constructed to replicate ILTS measurements in low-temperature plasmas, the presented method can be applied to ILTS measurements in high-temperature plasmas.

## Acknowledgements

This work was supported by a NASA Space Technology Graduate Research Opportunity (No. 80NSSC23K1217).

## **Author Contributions**

Julian Lopez-Uricoechea: Conceptualization (lead); Formal analysis (lead); Methodology (lead); Writing - original draft (lead); Writing - review and editing (equal). Mitchell L. R. Walker: Project administration (lead); Writing - review and editing (equal).

## Availability of data and materials

The data that support the findings of this study are available from the corresponding author upon reasonable request.

## References:

[1] V. Kolobov, V. Godyak, "Electron kinetics in low-temperature plasmas," Physics of Plasmas **26**, 060601, 2019.

- [2] G. J. M. Hagelaar, L. C. Pitchford, "Solving the Boltzmann equation to obtain transport coefficients and rate coefficients for fluid models," Plasma Sources Science and Technology 14, 722, 2005.
- [3] A. Alvarez Laguna, B. Esteves, A. Bourdon, P. Chabert, "A regularized high-order moment model to capture non-Maxwellian electron energy distribution effects in partially ionized plasmas," Physics of Plasmas **29**, 083507, 2022.
- [4] I. D. Kaganovich, Y. Raitses, D. Sydorenko, A. Smolyakov, "Kinetic effects in a Hall thruster discharge," Physics of Plasmas 14, 057104, 2017.
- [5] A. M. Castillo, K. Hara, "Loss cone effects and monotonic sheath conditions of a partially magnetized plasma sheath," Physics of Plasmas **31**, 030701, 2024.
- [6] S. R. Cranmer, A. J. Schiff, "Electron heat flux in the solar wind: generalized approaches to fluid transport with a variety of skewed velocity distributions," Journal of Geophysical Research: Space Physics 126, e2021JA029666, 2021.
- [7] E. Ahedo, S. Correyero, J. Navarro-Cavalle, M. Merino, "Macroscopic and parametric study of kinetic plasma expansion in a paraxial magnetic nozzle," Plasma Sources Science and Technology **29**, 045017, 2020.
- [8] A. Marin-Cebrian, E. Bello-Benitez, A. Dominguez-Vazquez, E. Ahedo, "Non-Maxwellian electron effects on the macroscopic response of a Hall thruster discharge from an axial-radial kinetic model," Plasma Sources Science and Technology 33, 025008, 2024.
- [9] J. L. Suazo Betancourt, N. Butler-Craig, J. Lopez-Uricoechea, A. M. Steinberg, M. L. R. Walker, "Laser Thomson scattering measurements indicate non-isothermal magnetic field lines in magnetically shielded Hall effect thrusters," Physics of Plasmas 31, 113106, 2024.

PLEASE CITE THIS ARTICLE AS DOI: 10.1063/5.0281503

- [10] D. A. Kuldinow, Y. Yamashita, K. Hara, "Ten-moment fluid model for low-temperature magnetized plasmas," Physics of Plasmas 31, 123506, 2024.
- [11] L. L. Alves, A. Bogaerts, V. Guerra, M. M. Turner, "Foundations of modelling of nonequilibrium low-temperature plasmas," Plasma Sources Science and Technology **27**, 023002, 2018.
- [12] V. A. Godyak, R. B. Piejak, B. M. Alexandrovich, "Measurement of electron energy distribution in low-pressure RF discharges," Plasma Sources Science and Technology 1, 36, 1992.
- [13] T. K. Popov, M. Dimitrova, P. Ivanova, J. Kovacic, T. Gyergyek, R. Dejarnac, J Stockel, M. A. Pedrosa, D. Lopez-Bruna, C. Hidalgo, "Advances in Langmuir probe diagnostics of the plasma potential and electron-energy distribution function in magnetized plasma," Plasma Sources Science and Technology 25, 033001, 2016.
- [14] M. Tichy, A. Petin, P. Kudrna, M. Horky, S. Mazouffre, "Electron energy distribution function in a low-power Hall thruster discharge and near-field plume," Physics of Plasmas 25, 061205, 2018.
- [15] T. I. Cox, V. G. I. Deshmukh, D. A. O. Hope, A. J. Hydes, N. S. Braithwaite, N. M. P. Benjamin, "The use of Langmuir probes and optical emission spectroscopy to measure electron energy distribution functions in RF-generated argon plasmas," Journal of Physics D: Applied Physics **20**, 820, 1987.
- [16] N. Bibinov, H. Halfmann, P. Awakowicz, "Determination of the electron energy distribution function via optical emission spectroscopy and a Langmuir probe in an ICP," Plasma Sources Science and Technology 17, 035004, 2008.

- [17] J. B. Boffard, R. O. Jung, C. C. Lin, A. E. Wendt, "Optical emission measurements of electron energy distributions in low-pressure argon inductively coupled plasmas," Plasma Sources Science and Technology 19, 065001, 2010.
- [18] A. Dwivedi, K. Hara, "Estimation of electron kinetics in low-temperature plasmas using data assimilation," Journal of Physics D: Applied Physics **58**, 175203, 2025.
- [19] L. Grimaud, A. Petin, J. Vaudolon, S. Mazouffre, "Perturbations induced by electrostatic probe in the discharge of Hall thrusters," Review of Scientific Instruments **87**, 043506, 2016.
- [20] M. Huang, K. Warner, S. Lehn, G. M. Hieftje, "A simple approach to deriving an electron energy distribution from an incoherent Thomson scattering spectrum," Spectrochimica Acta Part B: Atomic Spectroscopy **55** (9), pp. 1397-1410, 2000.
- [21] T. Hori, M. Kogano, M. D. Bowden, K. Uchino, K. Muraoka, "A study of electron energy distributions in an inductively coupled plasma by laser Thomson scattering," Journal of Applied Physics **83**, pp. 1909-1916, 1988.
- [22] B. Vincent, "Incoherent Thomson Scattering Investigations in Hall Thruster, Planar Magnetron and ECR Ion Source Plasmas," Ph.D. dissertation (Université D'Orléans, 2019)
- [23] J. L. Suazo Betancourt, S. J. Grauer, J. Bak, A. M. Steinberg, M. L. R. Walker, "Bayesian plasma model selection for Thomson scattering," Review of Scientific Instruments 95, 043004, 2024.
- [24] G. Zhuang, R. Behn, I. Klimanov, P. Nikkola, O. Sauter, "Influence of non-Maxwellian velocity distributions during ECRH and ECCD on electron temperature measurements by Thomson scattering," Plasma

PLEASE CITE THIS ARTICLE AS DOI: 10.1063/5.0281503

- [25] B. C. Foo, D. B. Schaeffer, P. V. Heuer, "Recovering non-Maxwellian particle velocity distribution functions from collective Thomson scattered spectra," AIP Advances 13, 115328, 2023.
- [26] A. L. Milder, S. T. Ivancic, J. P. Palastro, D. H. Froula, "Impact of non-Maxwellian electron velocity distribution functions on inferred plasma parameters in collective Thomson scattering," Physics of Plasmas **26**, 022711, 2019.
- [27] J. Zheng, C. X. Yu, Z. J. Zheng, "Effects of non-Maxwellian (super-Gaussian) electron velocity distribution on the spectrum of Thomson scattering," Physics of Plasmas 4, pp. 2736-2740, 1997.
- [28] Y. Y. Yamaguchi, "Nondiagonalizable and nondivergent susceptibility tensor in the Hamiltonian mean-field model with asymmetric momentum distributions," Physical Review E 92, 032109, 2015.
- [29] F. LeBlanc, D. Hubert, "A generalized model for the proton expansion in astrophysical winds. I. The velocity distribution function representation," The Astrophysical Journal **483**, 464, 1997.
- [30] A. A. Abid, M. Z. Khan, Q. Lu, S. L. Yap, "A generalized AZ-non-Maxwellian velocity distribution function for space plasmas," Physics of Plasmas **24**, 033702, 2017.
- [31] J. C. Raymond, P. A. Isenberg, J. M. Laming, "Non-Maxwellian proton velocity distributions in nonradiative shocks," The Astrophysical Journal **682**, 408, 2008.
- [32] A. L. Milder, J. Katz, R. Boni, J. P. Palastro,M. Sherlock, W. Rozmus, D. H. Froula,"Statistical analysis of non-Maxwellian electron

- distribution functions measured with angularly resolved Thomson scattering," Physics of Plasmas 28, 082102, 2021.
- [33] P. J. Roberts, B. A. Jorns, "Laser measurement of anomalous electron diffusion in a cross-fielded plasma," Physical Review Letters **132**, 135301, 2024.
- [34] L. B. Wilson III, L-J. Chen, S. Wang, S. J. Schwartz, D. L. Turner, M. L. Stevens, J. C. Kasper, A. Osmane, D. Caprioli, S. D. Bale, "Electron energy partition across interplanetary shocks. I. Methodology and data product," The Astrophysical Journal Supplement Series 243, 8, 2019.
- [35] P. J. Roberts, M. G. Allen, D. G. Brick, B. A. Jorns, "Empirical closures for momentum and energy transport in Hall thrusters based on Thomson scattering measurements," International Electric Propulsion Conference, IEPC-2024-393, Toulouse, 2024.
- [36] L. B. Wilson III, L-J. Chen, S. Wang, S. J. Schwartz, D. L. Turner, M. L. Stevens, J. C. Kasper, A. Osmane, D. Caprioli, S. D. Bale, "Electron energy partition across interplanetary shocks. II. Statistics," The Astrophysical Journal Supplement Series **245**, 24, 2019.
- [37] J Bak, J. L. Suazo Betancourt, A. Rekhy, A. Abbasszadehrad, R. B. Miles, C. M. Limbach, M. L. R. Walker, "High resolution spatially extended 1D laser scattering diagnostics using volume Bragg grating notch filters," Review of Scientific Instruments **94**, 023003, 2023.
- [38] M. J. van de Sande, "Laser scattering on low temperature plasmas: high resolution and stray light rejection," Ph.D. dissertation (Eindhoven University of Technology, 2022)
- [39] M. Hoffman, P. Sountsov, J. V. Dillon, "NeuTra-lizing bad geometry in Hamiltonian Monte Carlo using neural transport," arXiv:1903.03704 [stat.CO], 2019.

PLEASE CITE THIS ARTICLE AS DOI: 10.1063/5.0281503

[40] "Example: Neural Transport," NumPyro Documentation, 2019, https://num.pyro.ai/en/stable/examples/neutra.ht <u>ml</u>. [41] M. D. Hoffman, A. Gelman, "The No-U-

Turn Sampler: Adaptively setting path lengths in Hamiltonian Monte Carlo," Journal of Machine Learning Research 15, 1593-1623, 2014.

[42] "Bayesian Regression Using NumPyro," NumPyro Documentation, 2019, https://num.pyro.ai/en/latest/tutorials/bayesian r egression.html.

[43] A. L. Milder, A. S. Joglekar, W. Rozmus, D. H. Froula, "Qualitative and quantitative enhancement of parameter estimation for modelbased diagnostics using automatic differentiation with an application to inertial fusion," Machine Learning Science and Technology 5, 015026, 2024.

[44] G. Livadiotis, "Kappa distributions: Thermodynamic origin and generation in space plasmas," Journal of Physics: Conference Series **1100**, 012017, 2018.

[45] B. Vincent, S. Tsikata, S. Mazouffre, T. Minea, J. Fils, "A compact new incoherent Thomson scattering diagnostic for lowtemperature plasma studies," Plasma Sources Science and Technology 27, 055002, 2018.

[46] J. Lopez-Uricoechea, J. L. Suazo Betancourt, N. Butler-Craig, M. L. R. Walker, "Spatially resolved laser Thomson scattering measurements in a negative glow and cathode presheath to investigate a 1D sheath model," Physics of Plasmas 31, 033503, 2024.

[47] V. A. Godyak, R. B. Piejak, B. M. Alexandrovich, "Electron energy distribution function measurements and plasma parameters in inductively coupled argon plasmas," Plasma Sources Science and Technology 11, 525, 2002.